

Prompt Fission Neutrons in the $^{239}\text{Pu}(n, f)$ Reaction

P. Marini^{1,*}, J. Taieb¹, B. Laurent¹, G. Belier¹, A. Chatillon¹, D. Etasse², P. Morfouace¹,
M. Devlin³, J. A. Gomez³, R. C. Haight³, K. J. Kelly³, J. M. O'Donnell³, and K. T. Schmitt³

¹CEA, DAM, DIF, F-91297 Arpajon, France

²LPC Caen, ENSICAEN, Université de Caen,
CNRS/IN2P3, Caen, France

³P-27, Los Alamos National Laboratory,
Los Alamos, NM-87545, USA

(Dated: December 15, 2024)

Prompt fission neutron spectra from $^{239}\text{Pu}(n, f)$ were measured for incident neutron energies from 0.7 to 700 MeV at the Weapons Neutron Research facility (WNR) of the Los Alamos Neutron Science Center. A newly designed high-efficiency fission chamber was coupled to the highly segmented Chi-Nu array to detect neutrons emitted in fission events. The double time-of-flight technique was used to deduce the incident-neutron energies from the spallation target and the outgoing-neutron energies from the fission chamber. Prompt fission neutron spectra (PFNS) were measured with respect to ^{252}Cf spontaneous fission down to 200 keV and up to about 12 MeV for all the incident neutron energies with typical uncertainties well below 2% up to about 10 MeV outgoing-neutron energy. The general trend of PFNS is well reproduced by JEFF3.3 and ENDF/B-VIII.0 evaluations. Discrepancies were however observed for the low-energy part of the spectra, where evaluations overestimate the number of emitted neutrons. Neutron multiplicities and average kinetic energies as a function of incident-neutron energy are obtained experimentally with reported uncertainties below 0.4%. Neutron multiplicities disagree with some older datasets above 6 MeV, indicating the need of using a high-efficiency fission detector, which does not bias the data. The measured mean kinetic energies agree with the most recent data. Evaluations fairly reproduce the trend, but fail to reproduce the experimental values within their uncertainties.

I. INTRODUCTION

Observables related to prompt fission neutrons represent a key parameter for nuclear energy applications and technology, and provide valuable information on the fission process. As far as the applications are concerned, it has been recently shown that accurate predictions of nuclear criticality using neutron transport codes crucially depend on the underlying nuclear data, especially the fission-neutron spectrum [1]. While the accuracy of evaluated neutron multiplicities, $\bar{\nu}$, has improved in recent years, the experimental database of prompt fission neutron spectra consists of limited number of datasets, far less precise than those on the other key fission observables and often discrepant [2, 3].

For the $^{239}\text{Pu}(n, f)$ prompt fission neutron spectrum (PFNS) the situation is similar: the few experimental data sets that are available and adequate for an evaluation [4–13] are often not in agreement within quoted uncertainties [3, 14]. Moreover, there are large gaps in the experimental data for important parts of the outgoing-neutron spectra, i.e. below 1 MeV and above 8 MeV. These two regions of the PFNS are particularly challenging because of technical limitations (detection efficiency at low neutron energy and statistics at high energy). The high α activity of the ^{239}Pu isotope makes the measurement even more challenging to carry out.

Due to these deficiencies in experimental data, evaluated data files partially rely on models to predict the spectra. However, despite the considerable progresses in recent years, mi-

croscopic models are not yet able to precisely predict the fission observables, and in particular PFN spectra, because of the complex physical processes associated with the emission prompt of neutrons from fission of actinides. Phenomenological models, mainly based on the Madland-Nix approach [15], are then used to evaluate PFN spectra in the libraries. These models rely on parameters, tuned as best fits to the measured PFN spectra. However, it has been suggested that significant systematic errors could be present in the evaluated libraries, leading to a too hard PFNS [16]. In particular, according to Ref. [17], the PFN spectra of major actinides should have more neutrons below 1 MeV and fewer neutrons above about 6 MeV outgoing-neutron energies. Recently developed Monte Carlo Hauser-Feshbach models [18] point to the same direction. For the fast-neutron induced $^{239}\text{Pu}(n, f)$ reaction, recent data from Lestone and Chatillon [11–13] support current PFNS evaluations for outgoing energies between 1.5 and 10 MeV, and 0.5 and 8 MeV, respectively. But these data do not rule out the ideas proposed in Ref. [17] that there should be more prompt fission neutrons below 1 MeV and fewer above 10 MeV.

The open question on the high-energy tail of the spectrum has important implications also on the understanding of the fission process. Indeed, this part of the spectrum is very sensitive to the total excitation energy sharing at scission: the spectrum gets harder at higher excitation energy. While in the original Madland-Nix model [15, 19] a thermal equilibrium between the two nascent fragments at scission is assumed, a recent model [20–22] describes the fission process with a constant temperature level density, where each nascent fragment would be characterised by a temperature only dependent on the mass number of the fragment. This model naturally leads

* paola.marini@cea.fr

to an unexpected partitioning of the excitation energy when increasing the incoming neutron energy [20], which would affect the high-energy tail of the spectrum.

Our group has been involved since 2000's in PFNS measurements [12, 13, 23, 24], in the framework of a collaboration agreement between the US Department of Energy - National Nuclear Security Administration (DOE/NNSA) and the French Commissariat à l'énergie atomique et aux énergies alternatives - Direction des applications militaires (CEA-DAM). First experiments on PFN spectra of $^{239}\text{Pu}(n, f)$ were carried out in 2007 and 2008 [12, 13]. Since then special efforts in the development of a new experimental area, new detectors, and data collection procedures were made with the aim of improving the measured PFNS accuracy. In particular, a new fission chamber was developed, with a fission fragment detection efficiency better than 95%, despite the high α -activity of the sample. Such a feature is crucial to avoid any bias of the data associated to a particular range in angle or total kinetic energy. In this work, we present the results of the $^{239}\text{Pu}(n, f)$ PFNS measurements performed in 2017 at the Los Alamos National Laboratory (LANL). The goals of this experiment are: (i) to significantly improve the experimental accuracy of the measured PFNS, in particular in the low- and high-energy tails of the spectrum, in the 1 to 700 MeV incident neutron energy range; (ii) to produce PFNS data as a function of incident-neutron energy, for which few experimental data exist to date, (iii) to provide an independent measurement of emitted-neutron multiplicity and mean kinetic energy as a function of incident-neutron energies with high accuracy.

The paper is structured as follows: in Secs. II and III the experimental setup and the data analysis are presented, respectively. Section IV presents and discusses the obtained results, while Sec. V concludes.

II. EXPERIMENTAL SETUP

The experiment was carried out at the WNR facility [25, 26] at the Los Alamos National Laboratory. A white pulsed neutron beam, spanning an energy range from below 1 MeV to several hundreds of MeV, is produced by 800 MeV proton-induced spallation reactions on a tungsten target. The beam is delivered in 625 μs -long macropulses with an average frequency varying between 100 and 120 Hz. Each macropulse contains micropulses separated by 1.8 μs . A 5%-borated, 0.5 inch-thick polyethylene absorber is placed into the beam line to harden the spectra in order to reduce the so-called wrap-around effect, i.e. to minimize the number of slow neutrons ($\lesssim 650$ keV) reaching the fission target at the same time or after the fastest neutrons of the following pulse. The neutron beam is collimated along a flight path of about 20 m before impinging onto the ^{239}Pu fission target. The beam pipe right upstream from the experimental hall is placed under vacuum to limit neutron scattering on air.

Data were taken for 20 days of effective time with a fission rate of 150 s^{-1} .

The experimental setup (Fig. 1) couples the 54 Chi-Nu scintillator array [27] to a newly developed fission chamber

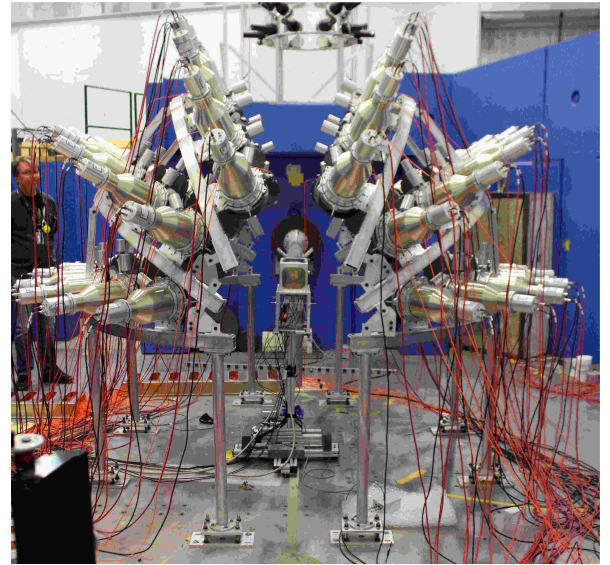


Figure 1. Photo of the experimental setup. The photo is looking upstream towards the spallation target.

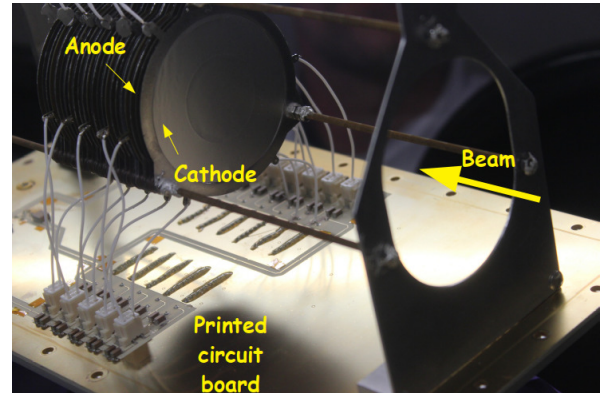


Figure 2. Photo of the interior of the fission chamber, showing the stacking of anodes and cathodes. The cathodes contain the ^{239}Pu deposits, the anodes are connected to the lower panel.

and a digital data acquisition system. The detectors are placed over a get-lost pit to minimize the amount of scattered neutrons on surrounding materials (see Sec. III C).

1. Fission chamber

The multi-plate fission chamber (Fig. 2) was designed to contain 47 mg of ^{239}Pu arranged in 22 deposits and 11 readout channels. The fissile material was deposited on every cathode, located 2.5 mm away from its corresponding anode. The diameter of each deposit was 33 mm and the isotopic purity of the material 99.90%. The chamber, filled with CF_4 gas to ensure a fast charge collection, operates 100 mbar above the local atmospheric pressure. This allows for a reduction in the amount of structural material, thereby minimizing the neutron scattering both for the incoming neutron beam and for

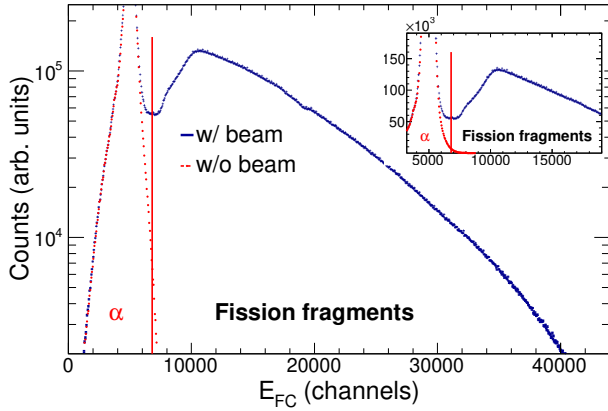


Figure 3. (Color online) Pulse height spectra of ^{239}Pu fission chamber obtained with (blue) and without (red) beam. The red line indicates the α -fission fragments threshold set in the data analysis (see Sec. III A 1).

the emitted fission neutrons (see Sec. III C). A more detailed description of the detector can be found in [28].

Dedicated front-end electronic boards containing pre-amplifiers and shapers were developed to match the detector characteristics. Thanks to the detector and electronics design, an improved α -fission fragment discrimination could be obtained, with a fission detection efficiency better than 95%, despite approximately 10 MBq α activity per channel. Two pulse height spectra (shown in Fig. 3) measured during the experiment with (in blue) and without (in red) beam illustrate the discrimination attained. A time resolution better than 0.8 ns full width at half maximum (FWHM) could be achieved. This leads to an emitted-neutron time-of-flight resolution of about 1.5 ns (FWHM). The latter arises from summed contribution of the fission chamber and the neutron detector time resolutions.

An identical chamber, containing a ^{252}Cf deposit, was used for neutron detection efficiency measurements (see Sec. III B).

2. Neutron detection array

The Chi-Nu neutron detector array [27] was used to measure neutrons in coincidence with a fission chamber signal. The Chi-Nu high-energy array consists of 54 EJ-309 liquid scintillator cells, read by photomultipliers, and arranged on a hemisphere with inner radius of about 1 m around the fission chamber, as shown in Fig. 1. The diameter and the thickness of each cell are 7 and 2 inches, respectively. The whole array covers close to 10% of the solid angle. The detectors are placed at nine different angles, with 6 detectors per angle, θ_{lab} , from 30° to 150° , with respect to the beam axis. The angular distribution of the emitted neutrons can therefore be studied. The use of the Chi-Nu array constitutes a significant improvement with respect to previous measurements [12, 13] performed with the FIGARO array, due to the higher number

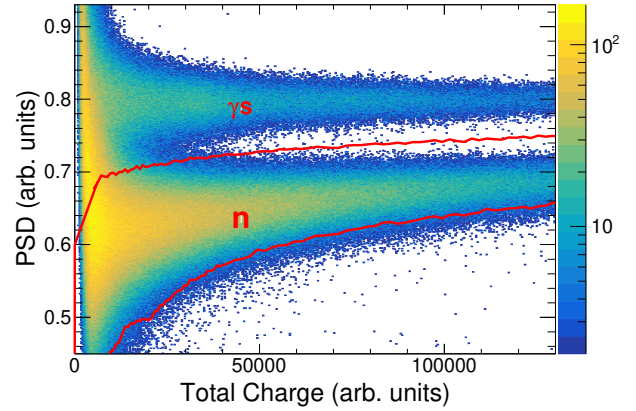


Figure 4. (Color online) Correlation between the pulse shape discrimination (PSD) and the total charge deposited in a cell by γ rays and neutrons. Signals falling into the red contour are associated to the detection of neutrons (see Sec. III A 2).

of scintillator cells.

The EJ-309 liquid scintillator is sensitive to both neutrons and γ -rays. Particle identification was performed via Pulse Shape Discrimination (PSD) technique, which is based on the charge integration of the slow and fast components of the pulse. Special care was devoted to the definition of the duration of the time integration windows in order to optimize the neutron- γ discrimination.

A 2 mm-thick Pb shield was placed in front of each cell to reduce the amount of low energy ($\lesssim 300$ keV) γ -rays, impinging on the cell. A typical pulse-shape discrimination plot is shown in Fig. 4, where the long to short pulse-component ratio (PSD) is plotted as a function of the total pulse charge. The use of the Pb shield allowed us to obtain a clear neutron- γ discrimination down to 30 – 40 keV electron equivalent energy [29].

3. Data acquisition system

Fast Acquisition System for nuclEAR Research The digital Fast Acquisition System for nuclEAR Research (FASTER) [30] was used during the experiment. Signals were digitized by a 500 MHz, 12-bits, low noise Analog to Digital Converter (ADC) and processed by real time numerical modules implemented into Field Programmable Gate Arrays (FPGA). The signal-to-noise ratio, as well as the zero time crossing determination on the Constant Fraction discriminator (CFD) signal, are optimized by limiting the analog bandwidth with the use of an input passive low pass filter (100 MHz). This allows to obtain a time resolution as low as 7.8 ps. The use of this acquisition system allowed the near complete avoidance of numerical dead-time. The acquisition was triggered and a coincidence window of $1.82\mu\text{s}$ opened when a signal was present in the fission chamber. Signals from the scintillators falling in the coincidence window were recorded. Events were then stored.

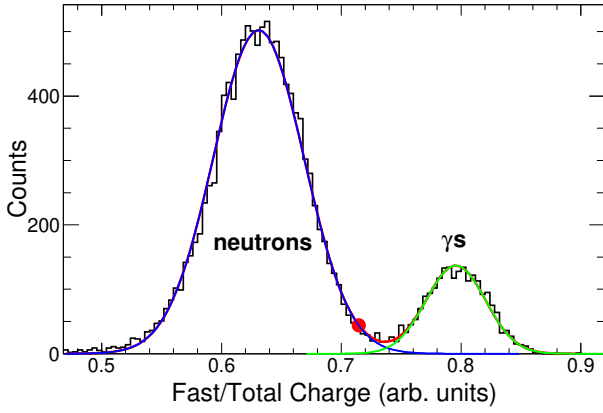


Figure 5. (Color online) Example of Gaussian fit of the short to total pulse components ratio for a given charge interval measured in one cell. The dotted blue curve is the fit of the neutron component, while the green line corresponds to the γ -ray component. The red dot indicates the position of the used threshold to discriminate neutrons and γ -rays. Selections were applied neither on incident-neutron energy nor on emitted-neutron energy.

III. DATA ANALYSIS

The experiment is based on the double time-of-flight technique. For each triggered event, the time-of-flight of the incoming neutron from the spallation target to the fission chamber and the time-of-flight of the emitted neutron from the fission chamber to the scintillator were measured. From the measured raw time-of-flight, the absolute time-of-flight for incoming and emitted neutrons were determined from the position of the γ -flash generated by the interaction of the proton beam on the tungsten target and from prompt-fission γ -rays, respectively. Distances between the fission target and each scintillator cell were carefully measured during the experiment with a high precision laser range meter with an uncertainty better than 0.2%. Given the importance of knowing the distance precisely, a careful consistency check of the measured values was performed at the very beginning of the analysis.

To measure the flight path length from the spallation source to each deposit in the fission chamber, a 0.5 inch-thick carbon absorber was inserted in the beamline upstream the experimental hall. The positions of the 2.08 and 6.3 MeV resonances in the total cross section gave the distances between each deposit of the fission chamber and the spallation target, with an absolute uncertainty of 4 mm over the 21.5 m flight path.

The combination of the time-of-flight and distance measurements gives us access to the incident and emitted neutron kinetic energies. The obtained relative uncertainty on the incident-neutrons energy is 0.08%. The uncertainty on the outgoing-neutron energy is dominated by the time-of-flight resolution (0.6 ns 1σ).

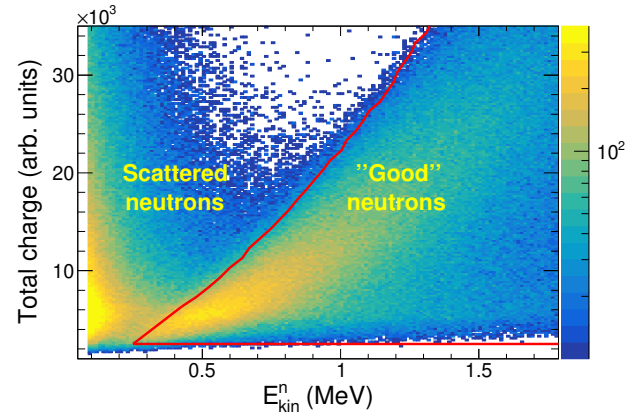


Figure 6. (Color online) Correlation between scintillator light output and kinetic energy, deduced from the time-of-flight measurement, of detected neutrons. The red contour selects “good neutrons” (see text).

A. Events selection

1. α -fission fragments discrimination

A threshold was set to discriminate fission from α -decay and nuclear reaction events in the fission chamber pulse-height spectrum (see Fig. 3). The threshold position is a compromise between minimizing the contribution of α -decay and reaction events and preserving the full fission-fragment total kinetic energy and angular distributions.

2. γ -neutron discrimination

Special efforts were made to improve the γ -neutron discrimination and γ -ray rejection. A first selection based on the detected time-of-flight was performed to remove prompt γ -rays. An additional selection was placed, for each neutron detector, on the PSD vs total charge correlation, shown in Fig. 4, to remove the remaining γ -rays. The cut was determined according to the procedure described in Ref. [31]: for each total charge interval, the short to total pulse-component ratio was fitted with two Gaussians, as shown in Fig. 5. This allowed us to define the cut with the same criterion for all the detectors and to estimate the remaining contribution of γ -rays, which is lower than 0.1%.

To remove a large fraction of scattered neutrons impinging on the detectors, a light output vs. outgoing-neutron kinetic energy correlation, as shown in Fig. 6, was made. Since a correlation exists between the kinetic energy of the neutron impinging on the scintillator cell and the scintillator light output, only events satisfying this correlation were selected (red contour in Fig. 6).

With these constraints, neutrons down to 200 keV could be identified. As these selections are applied both to ^{239}Pu and ^{252}Cf PFN spectra analysis, possible systematic uncertainties associated to the selections cancel out when correcting the

measured ^{239}Pu spectra for the neutron detector efficiency (see Sec. III B).

B. Neutron detector efficiency

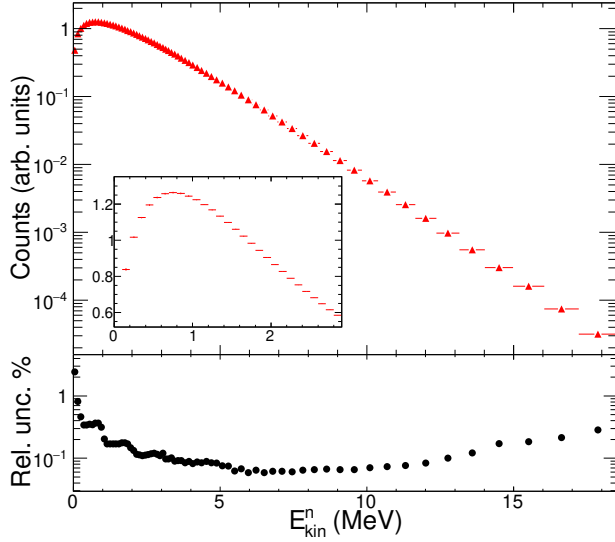


Figure 7. Evaluated ^{252}Cf PFNS [32], normalized to 3.7637 neutrons [33], used for neutron detection efficiency determination (see text). Horizontal bars indicate the width of the outgoing-neutron kinetic energy bins. In the insert a zoom of the low energy part of the spectrum is presented. The relative uncertainties are plotted in the lower panel.

Neutron detector efficiencies were obtained by measuring the PFNS of the ^{252}Cf spontaneous fission reaction in the same experimental conditions. For this purpose, beam-off runs were performed with a dedicated fission chamber containing a ^{252}Cf deposit placed on the central cathode of the chamber. All the structural materials constituting the ^{239}Pu fission chamber were present in the chamber used for the ^{252}Cf measurement. Fission signals triggered the data acquisition. The efficiencies were determined with respect to the Manhart evaluated PFNS standard [32], shown in Fig. 7, normalized to the evaluated standard $\overline{\nu}_{\text{tot}}$ of $(3.7637 \pm 0.42\%)$ for $^{252}\text{Cf}(\text{sf})$ [33]. In the following only the uncertainties present in the PFNS from Ref. [32] are propagated, while the uncertainty of 0.42% on $\overline{\nu}_{\text{tot}}$ is not accounted for. An example of the typical relative neutron detection efficiency is shown in Fig. 8. We stress that a threshold as low as 200 keV neutron energy could be obtained with the present setup.

C. Scattering corrections

The presence of structural and surrounding materials, and to a lesser extent air, causes the scattering of neutrons. The whole setup was placed above a 2 m “get-lost” pit, the beam pipe upstream from the experimental hall was placed under

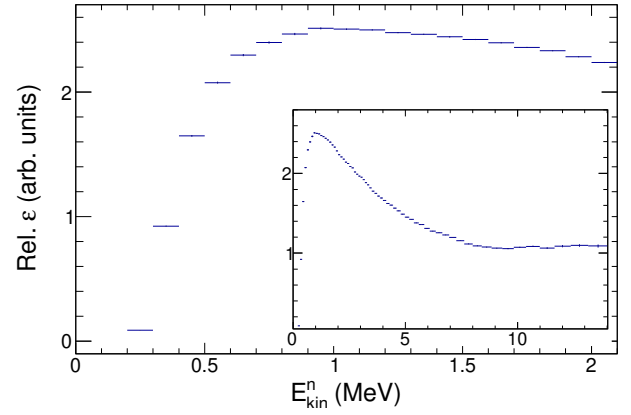


Figure 8. Measured mean relative efficiency as a function of the emitted neutron energy. The horizontal bars indicate the kinetic energy bin width. In the insert is shown the whole curve.

vacuum, and special efforts were dedicated to the development of the fission chamber with a reduced amount of scattering material (see Sec. II 1). Nevertheless, the remaining scattered neutron contributions have to be corrected for.

Scattering of prompt fission neutrons leads to an erroneous determination of their flight path, and thus of their kinetic energy. This contribution is accounted for, at a first order, when correcting the spectra for the detector efficiency. Indeed the efficiency measurement was performed in the same experimental conditions as the real measurement. Moreover, under the reasonable assumption that the ^{252}Cf and ^{239}Pu have similar PFN spectra, the distortions due to the remaining scattering events are compensated for in the efficiency calibration process.

The most significant contribution to background comes from scattered neutron beam and introduces a significant background in the PFNS. This background is not correlated with fission events, thus creating random coincidences in neutron detectors, and its contribution varies with time after the proton burst. A pulser trigger, acting as a fake-fission generator, was used to start the acquisition and record neutron-detector random coincidences during the whole experiment. As the beam was on, the various incident-neutron times-of-flight were randomly sampled and the background monitored as a function of the beam energy. The pulser rate was much higher than the rate of real fissions ($\approx 150 \text{ fissions} \cdot \text{s}^{-1}$), so that the statistical uncertainty associated to the background contribution was 4 times smaller than the statistical uncertainty associated to real fissions. An example of measured fission neutrons and random coincidence times-of-flight is shown in Fig. 9 in blue and red, respectively. It can be noted that for times-of-flight of about 20 and 150 ns (corresponding to energies of about 13 and 0.2 MeV, respectively) the difference between the measurement and the background vanishes, validating the correct background measurement and subtraction. Random coincidences were then subtracted offline.

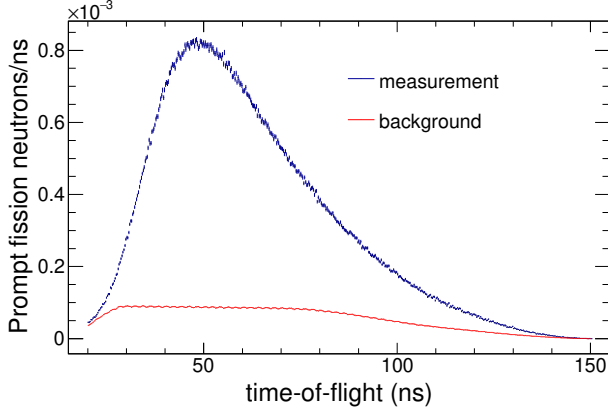


Figure 9. (Color online) Time-of-flight of emitted neutrons (blue) and associated background (red) measured for an incident neutron energy between 1.7 and 2.2 MeV and normalised to the number of events.

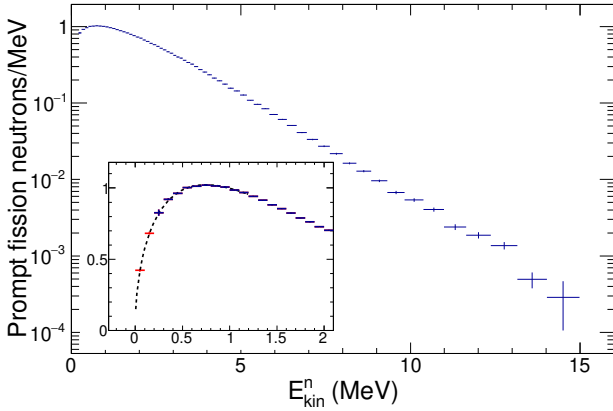


Figure 10. (Color online) PFNS for an incident neutron energy ranging from 0.7 to 1.2 MeV. When not visible uncertainties are smaller than symbols. In the insert is a zoom of the low energy part of the experimental spectrum (blue). The dashed line is the Watt-type fitted function and the red symbols are the extrapolated values below 200 keV.

D. Extraction of the PFNS

Thanks to the high statistics accumulated during the experiment and the low detection thresholds, PFNS from 200 keV to ~ 15 MeV could be extracted, the associated PFN observables studied, and their evolution investigated as a function of the incident neutron energy. Data were sorted in eighty-six incident neutron energy bins with energies ranging from 0.7 to 750 MeV. The bin widths were chosen based on the available statistics and on the incident-neutrons time-of-flight resolution. The bin width was 0.5 MeV at low incident neutron energies and it increases up to 20 MeV at 250 MeV. The used bin-widths are reported in Table I.

For each detector, time-of-flight spectra were measured for each incident neutron energy bin. The time spectra, corrected for random coincidences, were then converted into en-

E_{in} range (MeV)	E_{in} bin width (MeV)	E_{in} range (MeV)	E_{in} bin width (MeV)
0.7 – 6.2	0.5	26.4 – 32.4	3.0
6.2 – 9.4	0.8	32.4 – 82.4	5.0
9.4 – 20.4	1.0	82.4 – 252.4	10.0
20.4 – 26.4	1.5	> 252.4	20.0

Table I. Incident-energy bin widths used in the analysis.

ergy spectra and corrected for the detection efficiency normalized to the $^{252}\text{Cf(sf)}$ standard. The final spectrum for a given incoming-neutron energy range was finally obtained by combining all the detector spectra. In the following, results are presented with the absolute statistical and systematics error bars, propagated through the data analysis. The systematic uncertainty includes the uncertainty on the evaluated ^{252}Cf spectrum. The horizontal bars indicate the width of the emitted neutron energy bin and do not represent an error bar. The chosen variable bin width for the energy spectra is a compromise between a precise shape of the spectrum, enough statistics and the outgoing-neutron time-of-flight resolution.

An example of the measured prompt fission neutron spectra is shown in Fig. 10. The spectrum was obtained for an incident neutron energy ranging from 0.7 to 1.2 MeV, with a mean energy of 0.97 MeV. The performances of the setup and the associated electronics chain, and the high collected statistics, allowed PFN spectra to be experimentally measured from 0.25 MeV to 10-to-14 MeV, depending on the incident neutron energy, with uncertainties from 0.2% to 10% around 0.8 MeV and 12 MeV, respectively.

1. Extrapolation of PFNS at low kinetic energy

Despite the rather low outgoing-neutron energy threshold, it should be kept in mind that quantities such as the multiplicity of prompt fission neutrons, $\bar{\nu}$, is sensitive to the low-energy part of the spectrum. Owing to simple theoretical descriptions of PFNS based on either Watt [34] or Maxwellian [35] spectra, the measured spectra were extrapolated at energies from 0.2 MeV downwards by fitting the low energy part of the spectra with a Watt-type and a Maxwell-type distribution [36]. The Watt-based extrapolation was limited to incident energies below the opening of the second-chance fission, around 6 MeV. The fitting ranges were 0.20 – 1.2 MeV for the two functions. The uncertainties on the extrapolated points at 0.05 and 0.15 MeV were given by the uncertainties and covariances on the fit parameters. Consistent results were obtained below 6 MeV incident-neutron energy when using Watt-type and Maxwell-type distributions. This validates the use of a Maxwell-type distribution at energies above 6 MeV. An example of the result is shown in the insert in Fig. 10, where blue points are experimentally measured and red points are extrapolated. In the following we will refer to these extrapolated spectra as “spectra” and they will be used to calculate the quantities of interest, unless differently specified. As a

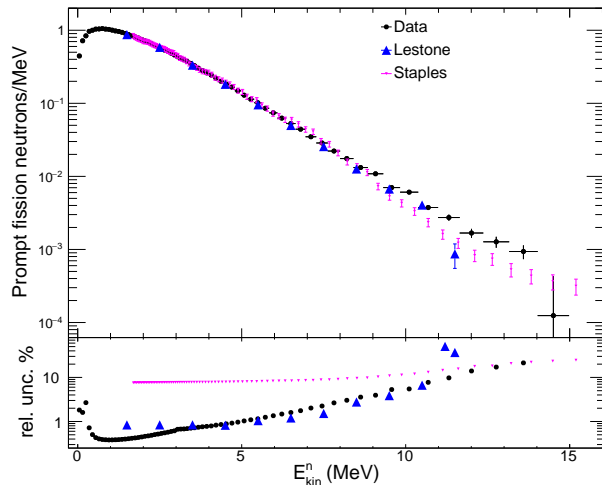


Figure 11. (Color online) Prompt fission neutron spectrum for an incident neutron energy ranging from 1.2 to 1.7 MeV (black squares) compared to data from Lestone et al. [11] (blue triangles) and from Staples et al. [9] (magenta triangles), measured at 1.5 MeV. In the lower panel the uncertainties of the three measurements are compared.

test case, the same extrapolation method was applied to identically truncated PFNS generated by the General Description of Fission Observables (GEF) code [37]. From the comparison of the extrapolated and the full distribution, we observe differences smaller than 0.1% on the total neutron multiplicity ($\bar{\nu}_{tot}$) and PFN mean kinetic energy, \bar{E} , thus validating the extrapolation method.

IV. RESULTS

A. PFNS

The PFNS measured for an average incident-neutron energy of 1.44 MeV is presented in Fig. 11 and compared to data from Lestone et al. [11] and Staples et al. [9] for 1.5 MeV incident energy. Our data are in very good agreement within the error bars with data from Lestone on the whole outgoing-energy range. It should be noted that results from Lestone were obtained from underground nuclear explosion measurements, with a much higher neutron flux on the studied sample. A good agreement is found also with data from Staples, with discrepancies above about 9 MeV, due to a change in the slope around 5 MeV, which leads to a softer spectrum. Similar conclusions can be drawn when comparing the spectrum measured at 2.5 MeV, provided as supplemental material, with the one measured by Staples.

In the lower panel of Fig. 11 the relative uncertainty on the spectrum is presented (black circles). This is a typical example of the attained accuracy in the measurement for the smallest incident energy bins (0.5 MeV bin width): between 0.3 and 5 MeV the uncertainty is smaller than 1%, it stays below 2% up to 7 MeV and it is less than 10% up to about

10 – 12 MeV. These values have to be compared to the uncertainties obtained by Lestone, which vary from 2 to 10% between 1.5 and 10.5 MeV, and to those measured by Staples, which are around 10% on the whole outgoing-energy range.

Figure 12 shows spectra for four incident neutron energy bins, compared to the ENDF/B-VIII.0 [38] and JEFF3.3 [39] evaluations. Spectra for the other energy bins are provided as supplemental material. All the spectra are normalized to the experimental neutron multiplicity obtained by integrating the PFNS on the whole energy range. Overall, a fair agreement is observed between the data and the evaluations. Slight discrepancies are found for the low- (< 1 MeV) and high-energy tails (> 9 MeV) of the spectra, depending on the incident neutron energy. We concentrate here on outgoing-neutron kinetic energies above 3 MeV. For spectra up to 3 MeV incident-neutron energy, predictions seem to underestimate the amount of fission neutrons above 9 MeV, as it was already observed in Ref. [13]. At the opening of the second-chance fission (≈ 6 MeV), a rather good agreement is observed between the data and the evaluations. For energies above the second chance fission, a better agreement is observed at high kinetic energy with the JEFF3.3 evaluation, while ENDF/B-VIII.0 predicts harder spectrum (a higher number of high-energy fission neutrons).

Figures 13 and 14 show the ratio of PFN spectra to a Maxwellian distribution with temperature $T = 1.32$ MeV for five incident-neutron energy bins, compared to ENDF/B-VIII.0 and JEFF3.3 evaluations. In Fig. 14 only emitted neutrons with kinetic energies below 8 MeV are shown, to focus the attention on the low-energy part of the spectra. At low incident-neutron energy the evaluations slightly underestimate the number of neutrons emitted with energy below 500 keV, while a better agreement is found from the opening of the second-chance fission. The situation changes at higher energies, where the evaluations clearly overestimate the number of low energy fission neutrons emitted.

B. Neutron angular distributions and multiplicity $\bar{\nu}$

The high statistics accumulated during the experiment and the Chi-Nu segmentation allows us to obtain a precise shape of the PFNS as a function of the neutron emission angle with respect to the beam direction (θ_{lab}) for each incident-neutron energy range studied. Nine spectra, one for each measured θ_{lab} , were therefore obtained by combining the six spectra associated to a given angle. The fission-neutron multiplicity for each θ_{lab} and incident-energy range, $\bar{\nu}(\theta, E_{in})$, was determined by integrating the spectra on the whole outgoing-neutron energy range. The angular distributions of prompt fission neutrons for six incident-energy ranges are plotted in Fig. 15 as a function of $\cos(\theta_{lab})$. The uncertainty on $\bar{\nu}(\theta, E_{in})$ is close to 0.3 %. The angular distributions exhibit two main characteristics: first, they are not isotropic, even at low incident energies, with a $\nu(0^\circ)/\nu(90^\circ)$ of about 1.1 below 10 MeV, in agreement with data for fission fragment anisotropy from Refs.[40–42]. The anisotropy arises from the fact that PFN carry angular momentum from fully accelerated fission fragments. Information on fission fragments angular momentum at scission could

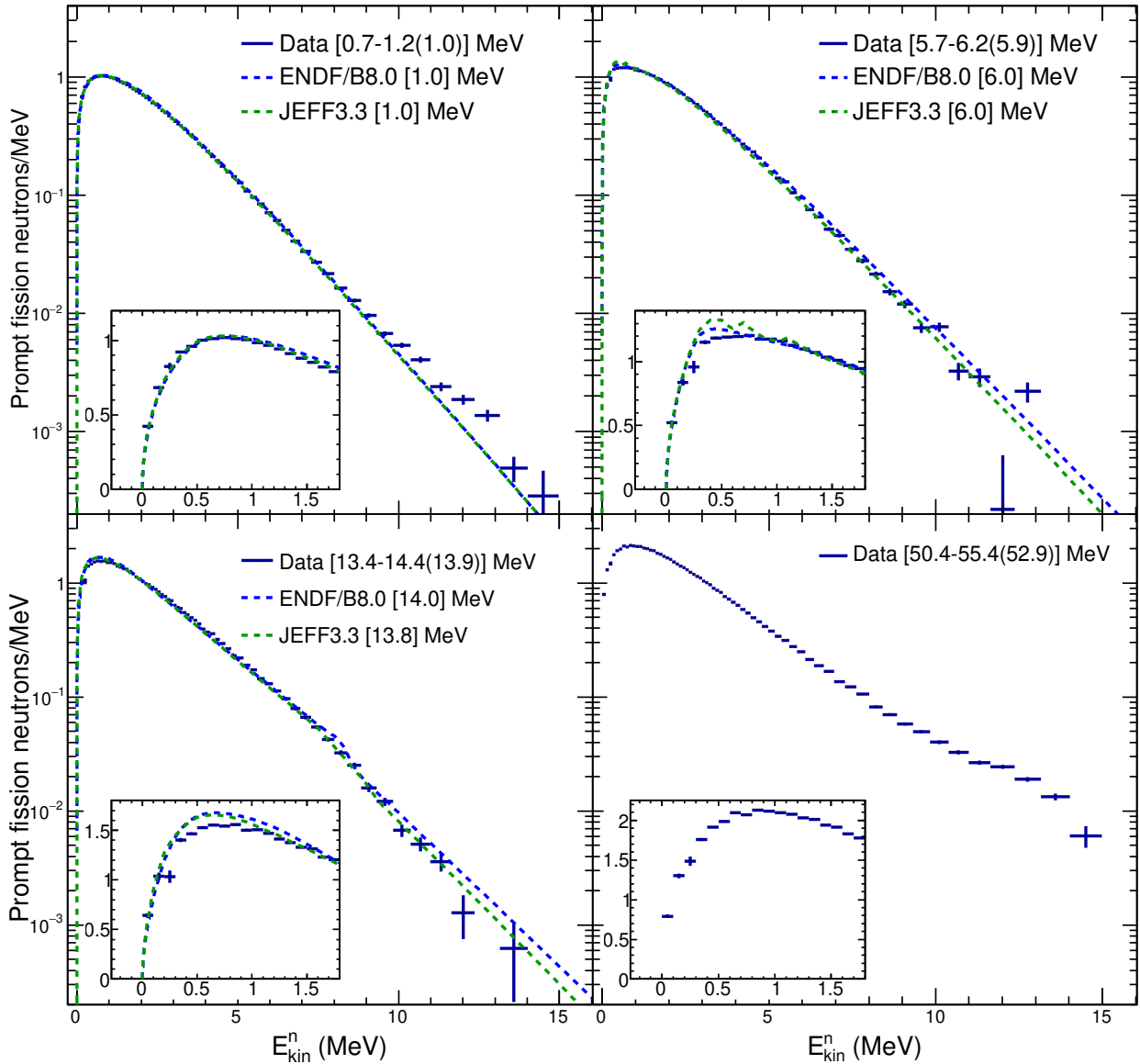


Figure 12. (Color online) Prompt fission neutron spectrum for four beam energy ranges, indicated among square brackets, together with the mean incident neutrons kinetic energy of each bin. Experimental data (crosses) are compared to the ENDF/B-VIII.0 (dotted blue line) and JEFF 3.3 (dashed green line) evaluations. A zoom of the low energy part of the spectra is shown in the inserts.

therefore be extracted by model comparison, which is beyond the scope of this paper. Second, angular distributions are characterized by a certain degree of forward/backward asymmetry which increases with the incident-neutron energy, reflecting the increase in the kinematical boost and pre-equilibrium emission.

The experimentally measured neutron angular distributions were also needed in the determination of the average neutron multiplicity, $\bar{\nu}(E_{in})$, for each incident neutron energy range. They were fitted with a 3rd-order polynomial and $\bar{\nu}(E_{in})$ was taken as the sum of the experimental values and the values deduced from the fitted distribution, for those angles that were not covered by detectors during the experiment. The uncer-

tainty contribution of the values deduced from the fitted distribution is negligible with respect to the uncertainty on the measured values. We stress that accounting for the neutron angular distribution and the most forward/backward angles modifies up to 3% the $\bar{\nu}$ values, as shown in Fig. 16. The contribution to the obtained $\bar{\nu}$ value of the low energy part of the spectrum, below 200 keV, where extrapolated values are considered (see Sec. IIID 1), is $\sim 3.5\%$ below 10 MeV and decreases for higher incident energy. Furthermore, possible not-measured double hits are accounted for. The probability of double-hit is determined, for the ^{252}Cf and the ^{239}Pu measurements, from the multiplicity distribution of hit detectors for every incident neutron energy bin. The double hit proba-

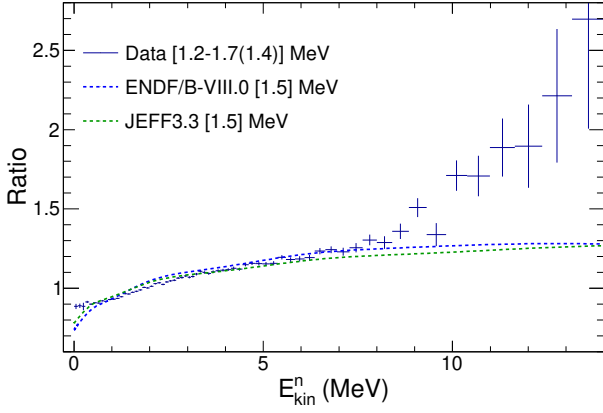


Figure 13. (Color online) Ratio of PFNS to a Maxwellian distribution with $T = 1.32$ MeV for a mean incident energy of 1.44 MeV. Experimental data (crosses) are compared to the ENDF/B-VIII.0 (dotted blue line) and JEFF 3.3 (dashed green line) evaluations.

bility for the ^{252}Cf measurement is 0.15% with a relative uncertainty of 0.09%. The net correction for $\bar{\nu}$ varies from 0.08% to 0.6% for incident energies from 1 to 700 MeV.

The obtained values are plotted in Fig. 17. Our data exhibit a constant increase up to 700 MeV with no fluctuations, as it can be seen in the insert of Fig. 17. The uncertainty spans from 0.12 to 0.27%, as a function of the incident-neutron energy and of the incident-energy bin-width used. At low incident neutron energy, below ≈ 14 MeV, $\bar{\nu}$ exhibits a linear dependence with the neutron energy, with a slope of (7.54 ± 0.08) MeV/n, and an extrapolated value of $\bar{\nu}$ at thermal neutron energies, $\bar{\nu}_{th}$, of (2.853 ± 0.004) , in agreement with the evaluated value of (2.878 ± 0.013) [33] within 2σ .

Some data from previous experiments, obtained using large volume liquid scintillator spheres, are also shown in the figure [43–46]. Our data are in good agreement within the error bars with the most recent and precise data, measured by Frehaut et al. [43], up to 6 MeV, while above this energy deviations up to 5% are observed. However there are two main differences in the used experimental methods. First, because of the granularity of the Chi-Nu array, the angular distribution of the emitted neutrons could be measured and $\bar{\nu}$ evaluated on the whole angular range, from 0 to 180° . This is not possible when using liquid scintillators balls. Moreover, the neutron-detection efficiency of a large liquid scintillator decreases as the angle θ_{lab} decreases [47], and the calculated fraction of neutrons escaping the detector ($\approx 10\%$) is sensitive to the assumed energy distribution of the prompt-fission neutrons, which was poorly known at the time of those measurements.

Our results are also compared to GEF calculations [37] and ENDF/B-VIII.0 and JEFF3.3 evaluations. The evaluations seem to overestimate $\bar{\nu}$ from very low incident energy, while GEF calculations predict a much steeper dependence of $\bar{\nu}$ as a function of the incident neutron energy than the measured one over the 0.7 – 14.4 MeV range.

For comparison, extrapolated values of $\bar{\nu}$ at thermal neutron energies, as well as the slope of $\bar{\nu}$ deduced from Frehaut data [43], GEF calculations and ENDF and JEFF evaluations

Fit range (MeV)	$\bar{\nu}(E_{th})$	slope (MeV/n)
0.7-14.4	2.855 ± 0.003	7.51 ± 0.03
0.7-6.2	2.853 ± 0.004	7.54 ± 0.08
Frehaut's data		
1.37-14	2.82 ± 0.01	6.62 ± 0.06
1.37-6	2.84 ± 0.02	7.00 ± 0.28
GEF		
0-6	2.76	6.92
ENDF/B-VIII.0		
0-6	2.851 ± 0.001	6.50 ± 0.13
JEFF3.3		
0-6	2.842 ± 0.001	6.16 ± 0.09
Evaluated values		
	2.878 ± 0.013 [33]	

Table II. Extrapolated $\bar{\nu}$ at thermal energies, $\bar{\nu}(E_{th})$, (2nd column) and slope of $\bar{\nu}$ (3rd column). Values are obtained from a linear fit to the data in the indicated incident neutron energy range (1st column).

are reported in Table II. While Frehaut's data present a slope change around the opening of the second-chance fission, the dependence of $\bar{\nu}$ as a function of the incident neutron energy in our data is linear in the 0 – 14 MeV range as for ENDF/B-VIII.0. Our $\bar{\nu}$ values extrapolated at thermal neutron energy are consistent within 2σ with the evaluation. This is the case neither for data from Ref. [43] nor for GEF predictions, ENDF/B-VIII.0 and JEFF3.3 evaluations.

C. PFN mean kinetic energy

The average neutron kinetic energy, \bar{E} , was computed from the spectra for every θ_{lab} and incident energy bin. No threshold was applied. An example of angular dependence of \bar{E} , $\bar{E}(\theta_{lab}, E_{in})$, is plotted in Fig. 18 for an incident neutron energy ranging from 2.7 to 3.2 MeV. The mean energy $\bar{E}(\theta_{lab}, E_{in})$ was fitted with a 3-order polynomial, weighting each $\bar{E}(\theta_{lab}, E_{in})$ for its associated neutron multiplicity $\bar{\nu}(\theta_{lab}, E_{in})$. Applying the same procedure used to determine $\bar{\nu}(E_{in})$, the average mean neutron energy $\bar{E}(E_{in})$ was taken as the sum of the experimental values and the values deduced from the fitted distribution, for those forward and very backward angles that were not covered by detectors during the experiment. Both the uncertainties on the neutron multiplicity, $\bar{\nu}(\theta_{lab}, E_{in})$, and on the mean energy, $\bar{E}(\theta_{lab}, E_{in})$, were propagated to determine the uncertainty on $\bar{E}(E_{in})$. The final uncertainty is estimated to be between 0.2% and 0.4% depending on the incident neutron energy bin.

The obtained values are plotted in Fig. 19 as a function of the kinetic energy of the incoming neutron. All available other experimental results are also plotted on the same graph [12, 13, 48, 49]. The kinetic energy of the emitted neutrons increases rather slowly over the full energy range, spanning

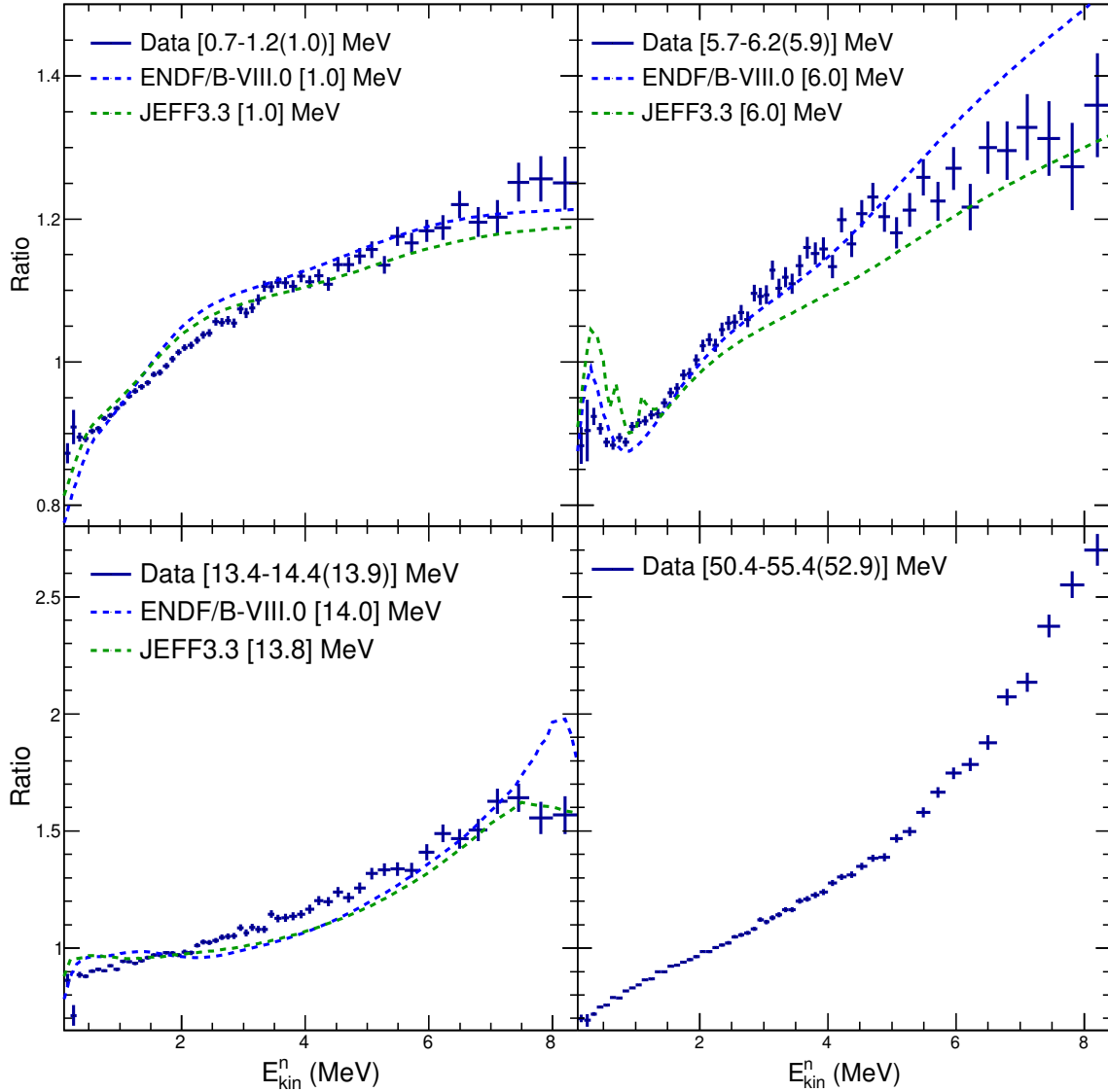


Figure 14. (Color online) Zoom below 8 MeV neutron kinetic energy of the ratio of PFNS to a Maxwellian-type distribution with $T = 1.32$ MeV for four beam energies ranges. Beam energies are indicated in square brackets, together with the mean incident neutrons kinetic energy of each bin. Experimental data (crosses) are compared to ENDF/B-VIII.0 (dotted blue line) and JEFF 3.3 (dashed green line) evaluations.

from 2.1 to 3.5 MeV. Above 20 MeV, we observe a slower increase of the kinetic energy, while fluctuations are observed below this energy. A clear dip of about 100 keV depth is observed around 6 MeV, and described with 8 experimental data points between 5 and 11 MeV. Smaller second and third dips are unambiguously observed around 14 and 20 MeV, as reported also in [12]. The presence of these dips is due to pre-fission neutrons emitted at the opening of the second- (third- and fourth-) chance fission. Indeed pre-fission neutrons, evaporated from the compound nucleus before fissioning, have smaller kinetic energy than fission neutrons, since they do not profit from the kinematical boost from fission fragments.

A very good agreement within error bars with the most recent data [12] is found up to 12 MeV. At higher energy, where pre-equilibrium reactions set in, the discrepancy is explained

by the fact that the setup used in Ref. [12] is most sensitive to lower energy evaporation neutrons and not to the higher energy neutrons emitted in the forward direction. A fair agreement is observed also with data from Refs.[13, 49], which present large error bars. Our data are not consistent with data from Ref. [48].

Figure 20 shows the comparison of our data to GEF predictions and ENDF/B-VIII.0 and JEFF3.3 evaluations. Below the opening of the second-chance fission GEF calculations and JEFF3.3 evaluation reproduce the trend of \bar{E} , although the values are slightly underestimated. On the contrary ENDF/B-VIII.0 indicates a steeper increase of \bar{E} with increasing the neutron energy, which is not observed in the data. Above 5 MeV JEFF3.3, and to a lesser extent ENDF/B-VIII.0, reproduce the dip depth, although they are not consistent with

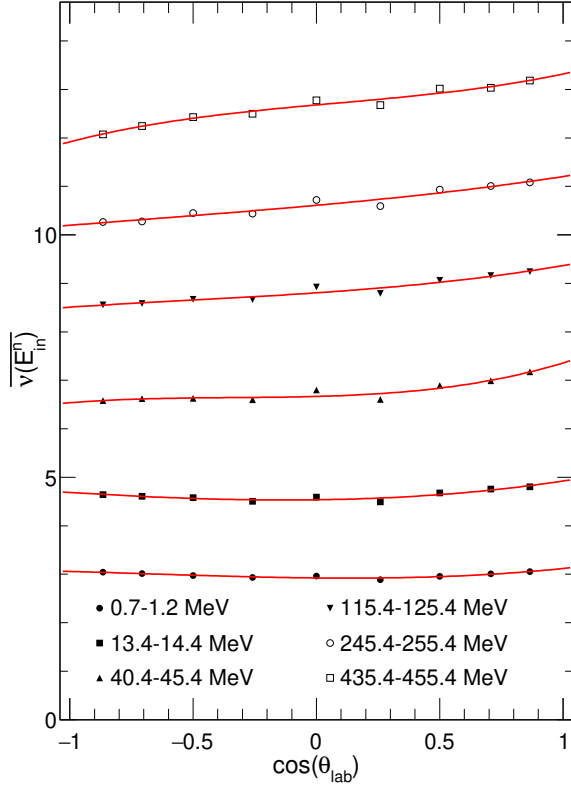


Figure 15. $\bar{\nu}(\theta, E_{in})$ for six incident-energy ranges. Uncertainties are smaller than symbols. Lines are fitted third-order polynomials (see text).

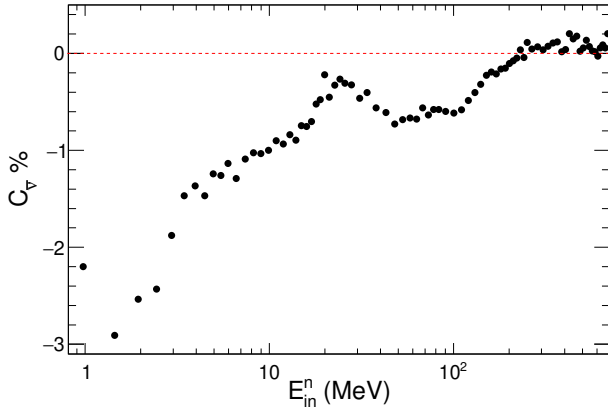


Figure 16. (Color online) Relative correction of $\bar{\nu}$ from the outgoing-neutron angular distribution as a function of the incident-neutron energy. The dotted red line is to guide the eyes.

the experimental values. Both evaluations indicate the presence of a second dip around 12 MeV, whose depth is much less pronounced in the experimental data than in the evaluations. It appears that all models and evaluations either underestimate (GEF) or overestimate the second and third chance fission probability in $^{239}\text{Pu}(n, f)$. These features notably impact the PFNS and the mean neutron energy. None of the

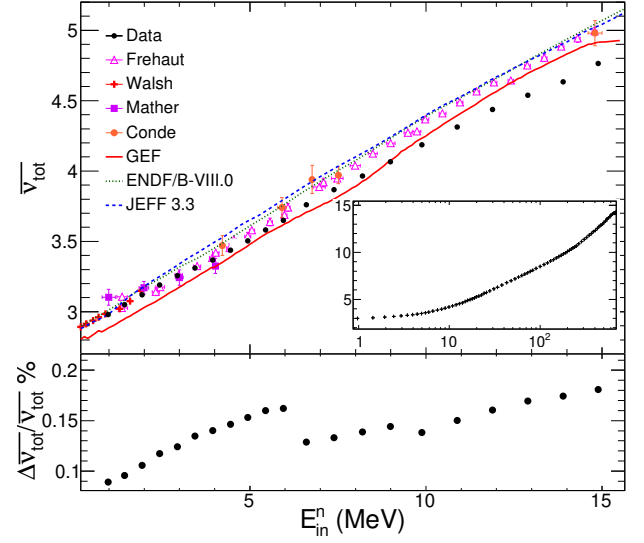


Figure 17. (Color online) Measured $\bar{\nu}$ as a function of incident neutron energy up to 15 MeV. Error bars are smaller than symbols. Some data from previous experiments are also reported [43–46]. Full, dotted and dashed lines are GEF calculations, and ENDF/B-VIII.0 and JEFF3.3 evaluations, respectively. In the insert is the measured $\bar{\nu}$ over all the studied incident neutron energies. In the lower panel is the absolute uncertainty on the measured $\bar{\nu}$.

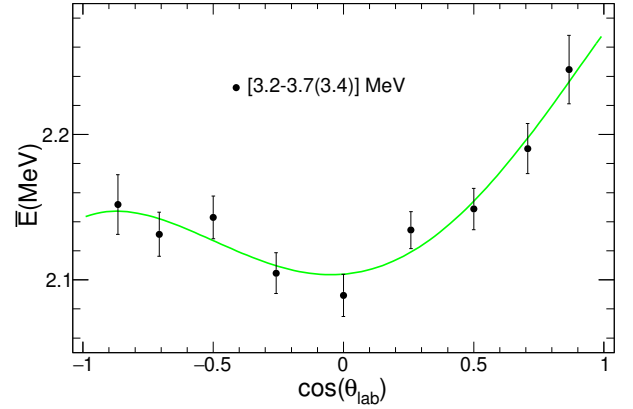


Figure 18. Angular dependence of $\bar{E}(\theta_{lab}, E_{in})$ for an incident neutron energy ranging from 3.2 to 3.7 MeV. The line is the best fit to the experimental data (see text).

evaluations is in agreement with the measured data. The GEF calculations fail in reproducing both the values and the trend of our data.

V. CONCLUSIONS

Prompt fission neutron spectra from 0.2 to 10 – 14 MeV outgoing-neutron energy were measured with the Chi-Nu array for incident neutron energies from 1 to 700 MeV. The obtained uncertainties are well below 2% for outgoing-neutron energies up to 7 MeV, and lower than the ones from all previ-

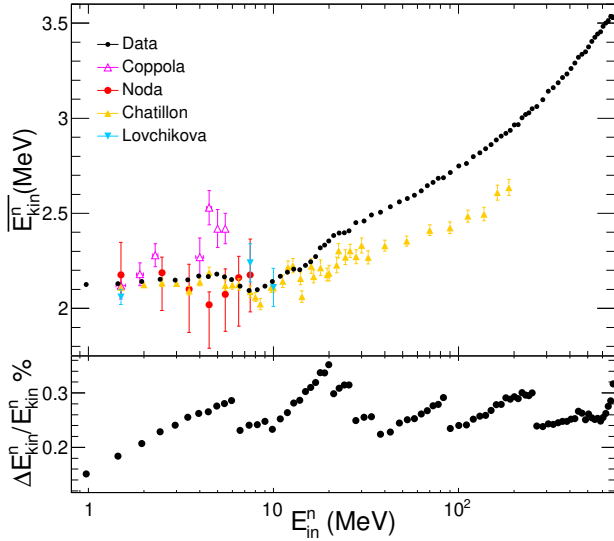


Figure 19. (Color online) Measured mean kinetic energy $\bar{E}(E_{in})$ of PFN as a function of incident neutron energy compared to data from previous experiments [12, 13, 48, 49] are also reported (panel a). Relative uncertainty on $\bar{E}(E_{in})$ a function of incident neutron energy (panel b).

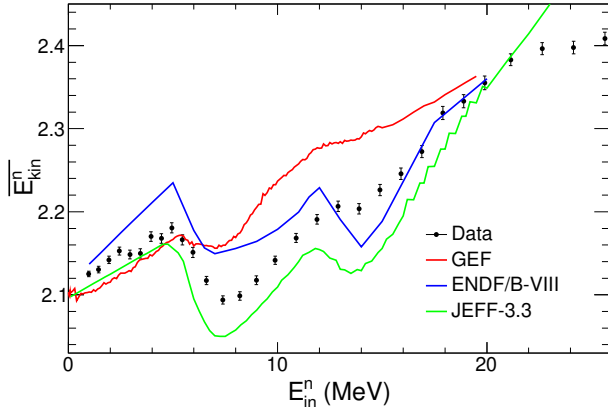


Figure 20. Measured mean kinetic energy $\bar{E}(E_{in})$ compared to GEF calculations and ENDF/B-VIII.0 and JEFF3.3 evaluations.

ous measurements.

In general, the data agree well with theoretical predictions based on the Los Alamos model, ENDF/B-VIII.0 and JEFF3.3, from 2 to about 10 MeV outgoing-neutron energies. Above 6 MeV incident energy, evaluations overestimate the number of low-energy neutrons, while in general a good agreement is found for the high-energy tail of the spectra.

The prompt neutron multiplicity was measured with an uncertainty better than 0.4% on the whole incident-energy range. A clear disagreement above 6 MeV with the most recent data from Frehaut as well as with the JEFF3.3 and ENDF/B-VIII.0 evaluations is found. However, our data extrapolated to thermal energies are in good agreement with the evaluated neutron multiplicity for thermal fission. Moreover a high efficiency detector for fission fragments detection was used to minimize the experimental bias, and the neutron anisotropy, measured with a highly segmented neutron detector, was accounted for. The availability, for the first time, of accurate experimental PFNS over a large incident-energy range opens up the possibility of a validation of the measured $\bar{\nu}$ values via integral measurements. Indeed ambiguities due to error compensations in these measurements could be solved exploiting the low energy part of the PFNS, which were accurately measured down to 0.2 MeV.

The mean energy of the PFNS was measured with a statistical uncertainty better than 0.4% for all incident neutron energies and shows a continuous increase with the beam energy. Signatures of the opening of the second- third- and fourth-chance fissions can be recognized around 7, 14 and 20 MeV. A good agreement is found with previous data from Ref. [12] up to the onset of pre-equilibrium reactions, around 10 – 12 MeV. The evaluations reproduce the shape, but not the measured values.

The obtained accuracies were made possible thanks to a newly developed fission chamber with a detection efficiency close to 100%, its associated electronics, the high statistics collected and the Chi-Nu segmentation and neutron/ γ discrimination capabilities. Given the success of the present experiment, further measurements should be performed to provide more accurate PFNS data than those available at present on other relevant actinides.

ACKNOWLEDGMENTS

We wish to acknowledge A. Moens, G. Sibbens and D. Vanleeuw from the JRC-Geel target preparation laboratory for providing ^{239}Pu samples and assisting their mounting in the fission chamber. We also wish to acknowledge the support of E. Bond from LANL target laboratory for providing the ^{252}Cf sample. This work was performed under the auspices of a cooperation agreement between CEA/DAM and DOE/NNSA on fundamental sciences and benefited from the use of the LANSCE accelerator facility. The work at Los Alamos was performed under the auspices of the U.S. Department of Energy by Los Alamos National Laboratory under Contract DE-AC52-06NA25396.

- [1] Y. Peneliau, O. Litaize, P. Archier, and C. De Saint Jean. *Nucl. Data Sheets*, 118:459 – 462, 2014.
- [2] R. Capote, V. Maslov, E. Bauge, T. Ohsawa, A. Vorobyev, M.B. Chadwick, and S. Oberstedt. Report consultants' meeting

on prompt fission neutron spectra. Technical report, Vienna, INDC(NDS) 0541, 2008.

- [3] D. Neudecker, T.N. Taddeucci, R.C. Haight, H.Y. Lee, M.C. White, and M.E. Rising. *Nucl. Data Sheets*, 131:289 – 318,

- 2016.
- [4] V. N. Nefedov, B. I. Starostov, and A. A. Boytsov. Precision measurements of ^{252}Cf , ^{233}U , ^{235}U and ^{239}Pu prompt fission neutron spectra (PFNS) in the energy range 0.04-5 MeV. In *IAEA Vienna Report INDC(CCP)-0457 (2014), translation into English from: Proceedings of the All-Union Conf. on Neutron Physics, Kiev, 2-6 Oct. 1983 2, 285 (1983) (in Russian), EXFOR-No. 40871*.
 - [5] A. A. Boytsov, A. F. Semenov, and B. I. Starostov. Relative measurements of $^{233}\text{U}+n_{th}$, $^{235}\text{U}+n_{th}$ and $^{239}\text{Pu}+n_{th}$ prompt fission neutron spectra (PFNS) in the energy range 0.01-5 MeV. In *IAEA Vienna Report INDC(CCP)-0459 (2014), translation into English from: Proceedings of the All-Union Conf. on Neutron Physics, Kiev, 2-6 Oct. 1983 2, 294 (1983) (in Russian), EXFOR-No. 40873*.
 - [6] B. I. Starostov, V. N. Nefedov, and A. A. Boytsov. Precision measurements of ^{252}Cf , $^{233}\text{U}+n_{th}$, $^{235}\text{U}+n_{th}$ and $^{239}\text{Pu}+n_{th}$ prompt fission neutron spectra (PFNS) in the energy range 2-11 MeV. In *IAEA Vienna Report INDC(CCP)-0458 (2014), translation into English from: Proceedings of the All-Union Conf. on Neutron Physics, Kiev, 2-6 Oct. 1983 2, 290 (1983) (in Russian), EXFOR-No. 40872*.
 - [7] B. I. Starostov, V. N. Nefedov, and A. A. Boytsov. Prompt neutron spectra from fission of ^{233}U , ^{235}U and ^{239}Pu by thermal neutrons and from spontaneous fission of ^{252}Cf in the 0.01-12 MeV energy range. In *IAEA Vienna Report INDC(CCP)-293/L, p.19-32 (1989), translation into English from: Yadernye Konstanty 1985, 16 (1985) (in Russian), EXFOR-No. 40930*.
 - [8] A. Lajtai, J. Kecskeméti, J. Sáfár, P. P. Dyachenko, and V. M. Piksaikin. Energy Spectrum Measurements of Neutrons for Energies 30 keV-4 MeV from Thermal Fission of Main Fuel Elements. In *Proceedings of the Conf. on Nuclear Data for Basic and Applied Sciences, Santa Fe 1985 1, 613 (1985), EXFOR-No. 30704*.
 - [9] P. Staples, J. J. Egan, G. H. R. Kegel, A. Mittler, and M. L. Woodring. *Nucl. Phys. A*, 591:41 – 60, 1995. EXFOR-No. 13982.
 - [10] H. H. Knitter. *Atomkernenergie*, 26:76, 1975. EXFOR-No. 20576.
 - [11] J. P. Lestone and E. F. Shores. *Nucl. Data Sheets*, 119:213 – 216, 2014.
 - [12] A. Chatillon, G. Bélier, T. Granier, B. Laurent, B. Morillon, J. Taieb, R. C. Haight, M. Devlin, R. O. Nelson, S. Noda, and J. M. O'Donnell. *Phys. Rev. C*, 89:014611, 2014.
 - [13] S. Noda, R. C. Haight, R. O. Nelson, M. Devlin, J. M. O'Donnell, A. Chatillon, T. Granier, G. Bélier, J. Taieb, T. Kawano, and P. Talou. *Phys. Rev. C*, 83:034604, 2011.
 - [14] R. Capote, Y.-J. Chen, F.-J. Hamsch, N.V. Kornilov, J. P. Lestone, O. Litaize, B. Morillon, D. Neudecker, S. Oberstedt, T. Ohsawa, N. Otuka, V.G. Pronyaev, A. Saxena, O. Serot, O.A. Shcherbakov, N.-C. Shu, D. L. Smith, P. Talou, A. Trkov, A. C. Tudora, R. Vogt, and A. S. Vorobyev. *Nucl. Data Sheets*, 131:1 – 106, 2016.
 - [15] D. G. Madland and J. Rayford Nix. *Nucl. Sci. Eng.*, 81:213–271, 1982.
 - [16] M.B. Chadwick, M. Herman, P. Obložinský, M. E. Dunn, Y. Danon, A. C. Kahler, D. L. Smith, B. Pritychenko, G. Arbanas, R. Arcilla, R. Brewer, D. A. Brown, R. Capote, A. D. Carlson, Y.S. Cho, H. Derrien, K. Guber, G.M. Hale, S. Hoblit, S. Holloway, T.D. Johnson, T. Kawano, B.C. Kiedrowski, H. Kim, S. Kunieda, N.M. Larson, L. Leal, J. P. Lestone, R. C. Little, E.A. McCutchan, R.E. MacFarlane, M. MacInnes, C.M. Mattoon, R.D. McKnight, S.F. Mughabghab, G.P.A. Nobre, G. Palmiotti, A. Palumbo, M.T. Pigni, V.G. Pronyaev, R.O. Sayer, A.A. Sonzogni, N.C. Summers, P. Talou, I.J. Thompson, A. Trkov, R.L. Vogt, S.C. van der Marck, A. Wallner, M.C. White, D. Wiarda, and P.G. Young. *Nucl. Data Sheets*, 112:2887 – 2996, 2011.
 - [17] V. M. Maslov, N. A. Tetereva, V. G. Pronyaev, A. B. Kagalenko, K. I. Zolotarev, R. Capote, T. Granier, B. Morillon, F.-J. Hamsch, and J.-C. Sublet. *J. Korean Phys. Soc.*, 59:1337, 2011.
 - [18] P. Talou, B. Becker, T. Kawano, M. B. Chadwick, and Y. Danon. *Phys. Rev. C*, 83:064612, 2011.
 - [19] D. G. Madland. *Acta Phys. Hungaria New Ser. Heavy Ion Phys.*, 10:231, 1999.
 - [20] K.-H. Schmidt and B. Jurado. *Phys. Rev. Lett.*, 104:212501, 2010.
 - [21] K.-H. Schmidt and B. Jurado. *Phys. Rev. C*, 83:014607, 2011.
 - [22] K.-H. Schmidt and B. Jurado. *Phys. Rev. C*, 83:061601, 2011.
 - [23] T. Ethvignot, M. Devlin, R. Drosch, T. Granier, R.C. Haight, B. Morillon, R.O. Nelson, J.M. O'Donnell, and D. Rochman. *Phys. Lett. B*, 575:221 – 228, 2003.
 - [24] J. Taieb, T. Granier, T. Ethvignot, M. Devlin, R.C. Haight, R.O. Nelson, J.M. O'Donnell, and D. Rochman. In *Proceedings of the International Conference on Nuclear Data for Science and Technology*, page 429, 2007.
 - [25] P. W. Lisowski, C. D. Bowman, G. J. Russell, and S. A. Wender. *Nucl. Sci. Eng.*, 106:208, 1990.
 - [26] P. W. Lisowski and K. F. Schoenberg. *Nucl. Instrum. Methods Phys. Res., Sect. A*, 562:910 – 914, 2006.
 - [27] R. C. Haight, H. Y. Lee, T. N. Taddeucci, J. M. O'Donnell, B. A. Perdue, N. Fotiades, M. Devlin, J. L. Ullmann, A. Laptev, T. Bredeweg, M. Jandel, R. O. Nelson, S. A. Wender, M. C. White, C. Y. Wu, E. Kwan, A. Chyzh, R. Henderson, and J. Gostic. *J. Inst.*, 7:C03028, 2012.
 - [28] J. Taieb, B. Laurent, G. Bélier, A. Sardet, and C. Varignon. *Nucl. Instrum. Methods Phys. Res., Sect. A*, 833:1 – 7, 2016. Patent pending for the anode concept.
 - [29] F. Pino, L. Stevanato, D. Cester, G. Nebbia, L. Sajo-Bohus, and G. Viesti. *Appl. Radiat. Isot.*, 89:79 – 84, 2014.
 - [30] FASTER. LPC-Caen <http://faster.in2p3.fr>, 2013.
 - [31] J. K. Polack, M. Flaska, A. Enqvist, C. S. Sosa, C. C. Lawrence, and S. A. Pozzi. *Nucl. Instrum. Methods Phys. Res., Sect. A*, 795:253 – 267, 2015.
 - [32] A. D. Carlson, V. G. Pronyaev, D. L. Smith, N. M. Larson, Zhenpeng Chen, G. M. Hale, F.-J. Hamsch, E. V. Gai, Soo-Youl Oh, S. A. Badikov, T. Kawano, H. M. Hofmann, H. Vonach, and S. Tagesen. *Nucl. Data Sheets*, 110:3215 – 3324, 2009.
 - [33] A. D. Carlson, V. G. Pronyaev, R. Capote, G. M. Hale, Z.-P. Chen, I. Duran, F.-J. Hamsch, S. Kunieda, W. Mannhart, B. Marcinkevicius, R. O. Nelson, D. Neudecker, G. Noguere, M. Paris, S. P. Simakov, P. Schillebeeckx, D. L. Smith, X. Tao, A. Trkov, A. Wallner, and W. Wang. *Nucl. Data Sheets*, 148:143 – 188, 2018.
 - [34] B. E. Watt. *Phys. Rev.*, 87:1037–1041, 1952.
 - [35] F. Bloch and H. Staub. U.S. Atomic Energy Commission Document AECD-3158. (as quoted by Terrell in *Phys. Rev.* 113:527–541, 1959), 1943.
 - [36] J. Terrell. *Phys. Rev.*, 113:527–541, 1959.
 - [37] K.-H. Schmidt, B. Jurado, C. Amouroux, and C. Schmitt. *Nucl. Data Sheets*, 131:107 – 221, 2016.
 - [38] D. A. Brown, M. B. Chadwick, R. Capote, A. C. Kahler, A. Trkov, M. W. Herman, A. A. Sonzogni, Y. Danon, A. D. Carlson, M. Dunn, D. L. Smith, G. M. Hale, G. Arbanas, R. Arcilla, C. R. Bates, B. Beck, B. Becker, F. Brown, R. J. Casperson, J. Conlin, D. E. Cullen, M.-A. Descalle, R. Firestone, T. Gaines, K. H. Guber, A. I. Hawari, J. Holmes,

- T. D. Johnson, T. Kawano, B. C. Kiedrowski, A. J. Koning, S. Kopecky, L. Leal, J. P. Lestone, C. Lubitz, J. I. Mrquez Damin, C. M. Mattoon, E. A. McCutchan, S. Mughabghab, P. Navratil, D. Neudecker, G. P. A. Nobre, G. Noguere, M. Paris, M. T. Pigni, A. J. Plompen, B. Pritychenko, V. G. Pronyaev, D. Roubtsov, D. Rochman, P. Romano, P. Schillebeeckx, S. Simakov, M. Sin, I. Sirakov, B. Sleaford, V. Sobes, E. S. Soukhovitskii, I. Stetcu, P. Talou, I. Thompson, S. van der Marck, L. Welser-Sherrill, D. Wiarda, M. White, J. L. Wormald, R. Q. Wright, M. Zerkle, G. zerovnik, and Y. Zhu. *Nucl. Data Sheets*, 148:1 – 142, 2018.
- [39] OECD/NEA. JEFF3.3 Evaluated data Library - Neutron Data. Technical report.
- [40] J. E. Simmons and R. L. Henkel. *Phys. Rev.*, 120:198–210, 1960.
- [41] D. L. Shpak, Yu. B. Ostapenko, and G. N. Smirenkin. *Sov. J. Nucl. Phys.*, 13:547, 1971.
- [42] A. S. Vorobyev, A. M. Gagarski, O. A. Shcherbakov, L. A. Vaishnene, and A. L. Barabanov. *JETP Letters*, 107:521–526, May 2018.
- [43] M. Soleilhac, J. Frehaut, and J. Gauriau. *Jour. of Nucl. En.*, 23:257 – 282, 1969.
- [44] R.L. Walsh and J.W. Boldeman. *Jour. of Nucl. En.*, 25:321 – 330, 1971.
- [45] D.S. Mather, P. Fieldhouse, and A. Moat. *Nucl. Phys.*, 66:149 – 160, 1965.
- [46] H. Cond, J. Hansn, and M. Holmberg. *Jour. of Nucl. En.*, 22:53 – 60, 1968.
- [47] R. Gwin, R. Spencer, and R. W. Ingle. *Nucl. Sci. Eng.*, 87:381, 1984.
- [48] M. Coppola and H. H. Knitter. *Zeitschrift fr Physik*, 232:286–302, 1970.
- [49] G. N. Lovchikova and A. M. Trufanov. In *Vop. At. Nauki Tekhn. Ser. Yadernye Konstanty*, page 102, 1996.